Chinese Chemical Letters 32 (2021) 1299–1308

Contents lists available at ScienceDirect

Chinese Chemical Letters

journal homepage: www.elsevier.com/locate/cclet

Review

Binder-free electrodes for advanced potassium-ion batteries: A review

Wencong Liu[a], Wenyi Liu[a], Yuqi Jiang[a], Qiuyue Gui[a], Deliang Ba[b], Yuanyuan Li[b], Jinping Liu[a,c,*]

[a] School of Chemistry, Chemical Engineering and Life Science, State Key Laboratory of Advanced Technology for Materials Synthesis and Processing, Wuhan University of Technology, Wuhan 430070, China
[b] School of Optical and Electronic Information, Huazhong University of Science and Technology, Wuhan 430074, China
[c] Key Laboratory for Photonic and Electronic Bandgap Materials, Ministry of Education, School of Physics and Electronic Engineering, Harbin Normal University, Harbin 150025, China

ARTICLE INFO

Article history:
Received 24 July 2020
Received in revised form 9 August 2020
Accepted 18 August 2020
Available online 20 August 2020

Keywords:
Binder-free
Free-standing electrode
Substrate-assisted directly grown electrode
Potassium-ion battery
Flexible device

ABSTRACT

Potassium-ion batteries (PIBs) have attracted enormous attention due to the abundance of potassium resources, low cost, fast ionic conductivity of electrolyte and relatively high operating voltage. Despite great efforts and progress, researches on PIBs are still at the initial stage, especially in the emerging field of flexible and wearable PIBs. The inevitable challenges for PIBs include low reversible capacity, unsatisfactory cycling stability and insufficient energy density, the solution to which mostly relies on designing advanced electrodes. Binder-free electrodes have emerged as promising electrode architecture for PIBs. Such electrodes avoid the use of insulating binders, which can be designed with various synergistic functional materials to address the aforementioned PIB issues and be endowed with flexibility/wearability. In this review, we mainly summarize the recent progress on binder-free electrodes for PIBs, with the focus on the methodologies, detailed strategies and functional materials for electrode construction. One strategy for binder-free electrodes is to assemble free-standing architecture with the help of carbon nanotubes (CNTs), graphitic fibers, and other carbon or mechanically robust materials, either alone or in combination. The other effective strategy is current collector substrate-assisted direct growth, including the use of carbon cloth, metal, MXenes and other conductive substrates. Additionally, challenges and research opportunities are put forward at the end as the guidance for future development of binder-free PIB devices.

1. Introduction

The global energy production is undergoing a rapid transition from traditional fossil fuels to clean and renewable energy resources such as solar and wind, which typically requires low-cost and high-performance energy storage systems to assist. As one of the best energy storage systems, rechargeable batteries have attracted great attention due to their low pollution, adjustable shape and size (from microbatteries to grid-scale systems), high efficiency and long cycle lifespan [1–4]. At present, lithium-ion batteries (LIBs) are dominating the market for portable energy storage in many electronics, including mobile phones and cameras, and are expected to be used in future electric vehicles and smart grids [5]. However, with the extensive applications, it is predicted that lithium reserves may be exhausted by 2025 [6]. Thus, concerns about the price and depletion of lithium resources have been accelerating the search for alternatives to rechargeable batteries in recent years [7,8].

In pursuit of alternatives to LIBs, other energy carriers (Na and K) of the same alkali series have been the focus of attention during the past years. Na and K are not only abundantly available but also distribute all around the world [9]. Moreover, PIBs and sodium-ion batteries (SIBs) share the same working principle as their counterpart of LIBs, which implies the feasibility to apply the research concepts and methodologies in LIBs to PIBs and SIBs. When further comparing these two emerging batteries, PIBs even demonstrate electrochemical superiority in some aspects (Table 1) [1,10]. For instance, K^+ generally has the smallest desolvation energy in PC and the highest ionic conductivity in EC/EDC-based electrolytes as compared to Na^+ and Li^+, which is beneficial to achieve facile insertion and diffusion of ion in batteries [11,12]. In addition, different from Na^+, K^+ can be intercalated into the well-

* Corresponding author at: School of Chemistry, Chemical Engineering and Life Science, State Key Laboratory of Advanced Technology for Materials Synthesis and Processing, Wuhan University of Technology, Wuhan 430070, China.
E-mail address: liujp@whut.edu.cn (J. Liu).

https://doi.org/10.1016/j.cclet.2020.08.032
1001-8417/

Table 1
Comparison of the properties of "lithium", "sodium" and "potassium" for rechargeable batteries [1,4].

Properties	Li^+	Na^+	K^+
Atomic mass	6.94	22.99	39.09
Ionic radii (Å)	0.76	1.02	1.38
Melting point (°C)	180.5	97.7	63.4
E^0 *vs.* SHE (V)	−3.04	−2.71	−2.93
E^0 *vs.* Li^+/Li in PC (V)	0	0.23	−0.09
Desolvation energy in PC (kJ/mol)	215.8	158.2	119.2
Ionic conductivity of the electrolyte of 1 mol/L MFSI in EC/EDC (mS/cm)	9.3	9.7	10.7
Theoretical capacity of graphite (mAh/g)	372	–	279
Reaction voltage of graphite *vs.* M^+/M (V)	~0.1	0.01 for hard carbon	~0.2
Abundance in the Earth's crust (mass%)	0.0017	2.3	1.5
Cost of carbonate (US$/ton)	23000	200	1000
Cost of industrial grade metal (US$/ton)	100000	3000	13000

known commercial graphite anode at room temperature with reversible capacities in excess of 200 mAh/g; the intercalation potential (~0.2 V *vs.* K/K^+) is low and comparable to that of Li^+ intercalation, which gives rise to high voltage of graphite-based PIBs [13]. With the aforementioned merits, PIBs have manifested even comparable comprehensive performance to LIBs in some cases. On the other hand, the low standard electrochemical potential of K/K^+ (lower than that of Na/Na^+ and comparable to that of Li/Li^+) has stimulated the development of potassium metal batteries, which share the same cathode materials to PIBs; thus the achievements in potassium metal batteries also facilitate the PIBs design [11,14,15].

However, the larger ionic radius of K^+ makes the insertion/deinsertion difficult in a variety of potential electrode materials of PIBs, resulting in limited capacity, poor rate performance and short cycle lifetime of PIBs [10]. Similar challenges take place in the alloying and conversion reactions, *i.e.*, large volume changes and severe side reactions, which result in low Coulombic efficiency (CE) and fading electrochemical performance. To address these issues, many efforts have been made to adjust the chemical composition, tailor the structure, and regulate the morphology of electrode materials [16]. In addition to these strategies, the innovation of the electrode architecture of PIBs is also much effective [17], due to the expanding pursuit of modern electronic systems like roll-up display, wearable devices and medical/implantable equipment, *etc.* [18]. It is of great significance to prepare functional, lightweight, flexible and even stretchable energy storage electrodes and devices. However, conventional electrodes are fabricated by mixing slurry of the active materials, conductive carbon and insulating binders, and then casting the slurry on metal foil. This method may not maintain good structural integrity during repeated mechanical deformation (bending, twisting, stretching, *etc.*) due to the weak physical adhesion between current collectors and electrode materials [19,20]. In contrast, binder-free electrodes could exactly overcome this problem and they can also be designed with tunable composition, structure and morphology to boost the K^+ storage. There are some other advantages as follows: (i) Binder-free electrodes avoid the step of slurry preparation, especially the mechanical blending process, which always destroys the as-formed nanostructures; (ii) Such electrode configuration provides more direct charge transport pathway and greatly exposes the active sites. Thus, it is possible that each individual nanostructure participates in electrochemical reactions, ultimately improving the specific capacity; (iii) Without binder and additives, the inactive components that will decrease the specific capacity are avoided; the interfaces within electrodes are also reduced, which helps to minimize the side reactions with electrolyte and increase the charge storage efficiency [16,21].

In this review, we will summarize recent progress in the design and fabrication of binder-free electrodes for PIBs. We focus on the preparation methods and functional materials of various binder-free electrodes. Generally, the methods of synthesizing binder-free

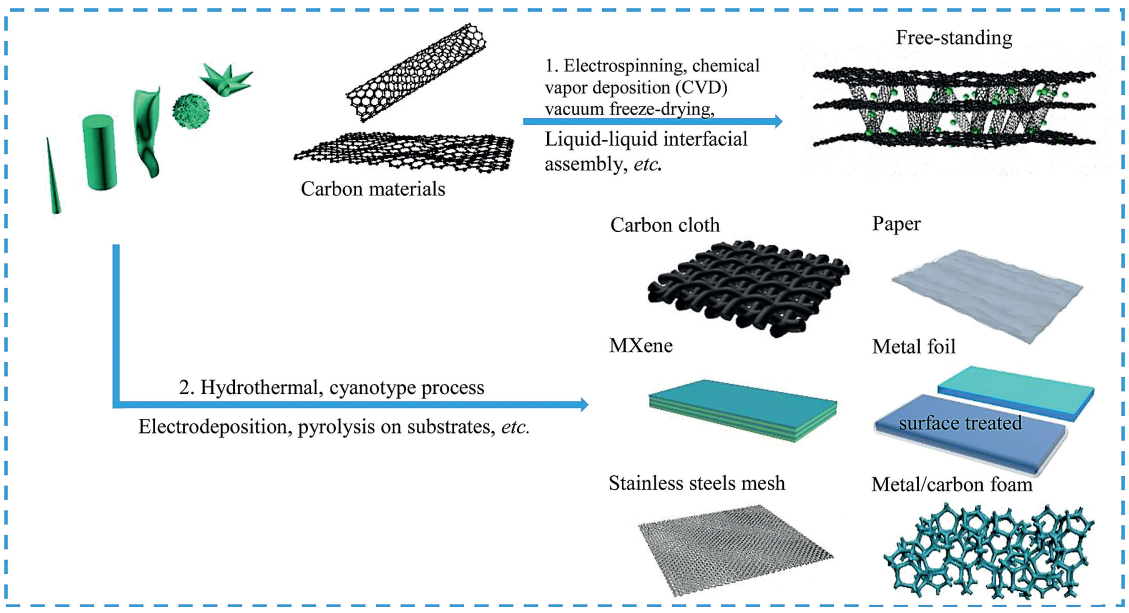

Fig. 1. Illustration of the two main strategies of fabricating binder-free electrodes for PIBs.

electrodes can be divided into substrate-free and substrate-assisted ones, as shown in Fig. 1. In terms of substrate-free strategy, nanostructured electrode materials are usually combined with a graphitic/carbon framework (one-dimensional (1D) fibers or yarns, two-dimensional (2D) films and three-dimensional (3D) foams or arrays) to form a free-standing electrode, and appropriate doping (N, O, Cl, *etc.*) into the carbon materials is basically utilized to improve potassium storage performance. For the current collector substrate-assisted strategy, the electrode materials are in-situ grown or coated on flexible substrates of carbonaceous materials, metal foils, and so on. Different kinds of active materials in the binder-free electrodes of PIBs will be discussed. At the end, the present review will provide the possible research directions for the future development of binder-free PIBs, which will also guide the design of other binder-free electrochemical energy storage devices.

2. Substrate-free methods for the preparation of binder-free electrodes

2.1. Graphene based free-standing electrodes

Graphene is generally regarded as an ideal material for energy storage due to its excellent conductivity, high chemical and thermal stabilities, exceptional mechanical flexibility, large specific surface area and ultralow weight. Beneficial from these merits, graphene has been extensively applied either alone or in combination with some active materials to form binder-free and free-standing electrodes for PIBs, which generally exhibited superior flexibility and mechanical robustness to conventional electrodes [16,22,23].

Bare 2D reduced graphene oxide (rGO) has excellent flexibility, good film-formation ability and large interlayer distance (3.66 Å) that enables a direct storage capability of K^+ (2.76 Å in diameter) (Fig. 2a) [24]. Wang *et al.* reported for the first time that K^+ can electrochemically intercalate into rGO at ambient temperature and pressure. They synthesized rGO film using the modified Hummer's method and used it directly as PIB anode without using any binder, carbon additives and current collector. Due to the rich surface functional groups of rGO, the rGO film electrode delivered the first charge capacity of 222 mAh/g with CE of ~50% at 5 mA/g (Fig. 2b), and a capacity of 150 mAh/g after 175 cycles at 10 mA/g. This work showed the possibility of the application of rGO film as binder-free electrode for PIBs. However, the electrochemical performance of rGO was not fully manifested. One main reason was the barriers for electron transport and ion diffusion in the cross-plane direction once graphene sheets have been tightly restacked to form the film structure. Thus, much work has been done to modify graphene, such N doping, S doping and B doping, *etc.* to increase the electrostatic repulsion of graphene sheet layer so as to reduce the agglomeration of graphene and improve the conductivity [25]. And apart from these chemical ways to improve the electrochemical performance of graphene for PIBs, Peng's group suggested an intriguing hybrid way to increase the interlayer spacing of graphene film *via* CNTs, as schematically depicted in Figs. 2c-e [26]. Because of 1D structure and high electrical conductivity, CNTs

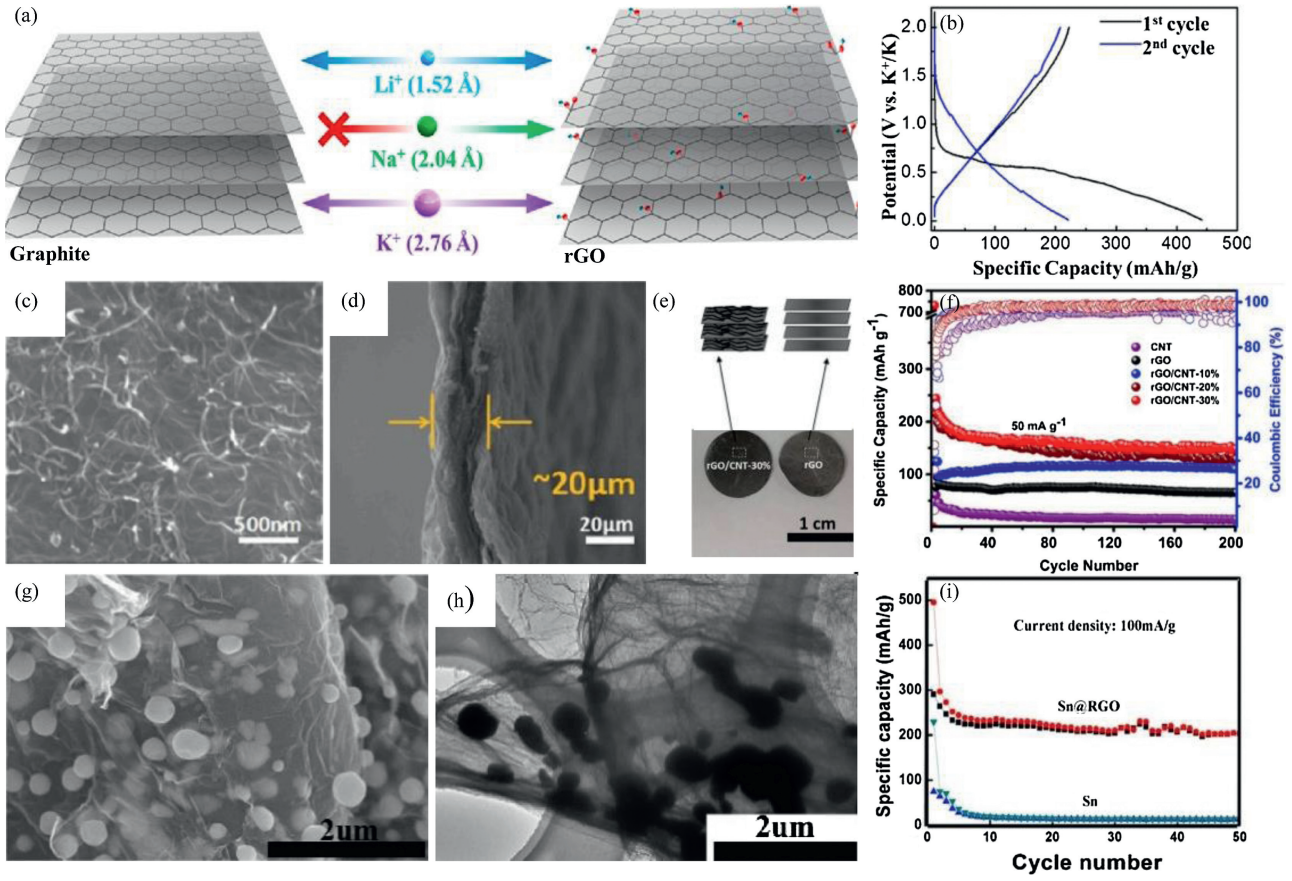

Fig. 2. (a) Schematic illustration of electrochemical intercalation of Li, Na and K ions into graphite and rGO. (b) The charge-discharge curves of rGO. Copied with permission [24]. Copyright 2015, American Chemical Society. (c, d) Top-view and cross-sectional scanning electron microscope (SEM) images of rGO/CNT-30% free-standing papers. (e) Typical digital photographs of the papers. (f) Cycling performance and Coulombic efficiency of rGO and rGO/CNT hybrid papers. Copied with permission [26]. Copyright 2019, Elsevier. (g, h) SEM and transmission electron microscope (TEM) images and (i) the cycling performance of Sn@rGO anode. Copied with permission [28]. Copyright 2018, Elsevier.

helped to bridge graphene layers and thus produced a 3D conductive carbon network, which not only boosted the cross-plane electrical conductivity, but also facilitated the K^+ diffusion. In addition, the hybrid electrode maintained the high flexibility and mechanical strength of graphene-based carbon papers, in which rGO/CNT-30% paper can deliver a capacity of 148 mAh/g after 200 cycles at a current density of 50 mA/g (Fig. 2f).

rGO can also be assembled into 3D networks with highly porous and wrinkle structure, which are favorable to accommodate volume expansion, inhibit self-aggregation of electrode nanoparticles and promote electron transfer [27]. Considering this, in principle, various free-standing 3D rGO-metal oxide or alloy hybrid electrodes can be designed for PIBs. For instance, Wang's group reported rGO network encapsulated tin-based submicron particles (Sn@rGO) as anodes for PIBs [28]. Due to the presence of the 3D interconnected porous rGO architecture (Figs. 2g and h), more active sites and high Brunauer–Emmett–Teller (BET) surface area (136.5 m^2/g) were attained for K^+ storage and Sn accommodation, respectively. As shown in Fig. 2i, at the current density of 100 mA/g, Sn@RGO revealed a specific charge capacity of 200 mAh/g after 50 cycles, which was much higher than that of the pure Sn electrode with only a charge capacity of 12.9 mAh/g. The concept reported in this work is general and can be applied to other alloy and conversion electrodes of PIBs that intrinsically suffer huge volume variation and structure pulverization during K^+ storage process.

However, the research on graphene-based free-standing electrodes for PIBs is in its infancy and there are still some limitations: (1) The uniform dispersion of graphene is difficult. Due to the strong π-π interaction and van der Waals force from interlayers, graphene layers usually have a natural tendency to restack, preventing full utilization of surface area and blocking electrolyte access; (2) The *in-situ* homogenous hybridization of rGO and other active materials is still challenging [29]. In future, novel techniques need to be developed to hybridize rGO with various metal compounds in simplified steps to form free-standing electrodes on large scale.

2.2. CNTs based free-standing electrodes

Thanks to their excellent conductivity (103 S/cm), good mechanical properties and high surface area (1600 m^2/g), 1D-tubular structure CNTs made from graphene layers have also been investigated both as supporting substrates and active materials to design free-standing electrodes for binder-free PIBs [30,31]. The unique merits of CNTs are the ultra-long length dimension that makes them easy to form 3D film with strong interconnections and the abundant inner and outer tubular surface for immobilization of exotic materials.

Similar to rGO, CNTs with free-standing and network architectures can be directly applied to PIBs. Zhao's group designed the nitrogen-doped cup-stacked CNT (NCSCNT) as the anode with open layer alignment structure for PIBs by vacuum filtrating CVD-grown method [32] (Fig. 3a). The obtained NCSCNT was directly used as the PIB anode without any binders and additional conductive agents. The open edge at the rim of the carbon cups from the nitrogen doping (Fig. 3b) was expected to enable K^+ ions to intercalate between graphene layers. Moreover, the interconnected network of the NCSCNT mats maintained its integrity architecture without cracks and fragments during repeated cycling, thereby retaining the ion/electron kinetics and cycling

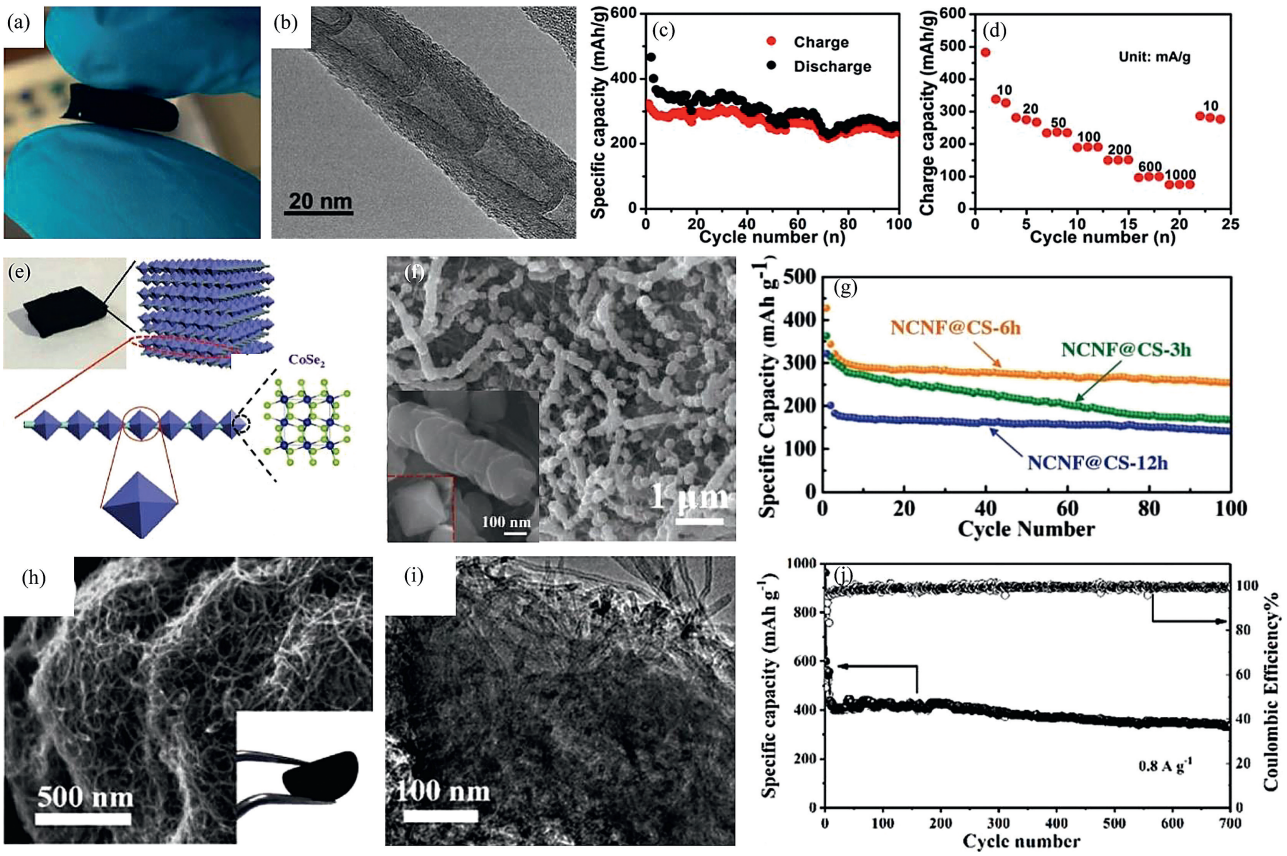

Fig. 3. (a) Digital photograph and (b) TEM image of NCSCNT. (c) Cycling stability and (d) rate performance of the NCSCNT anode. Copied with permission [32]. Copyright 2018, American Chemical Society. (e) Schematic illustration of the structure of flexible NCNT@CS. (f) SEM images of NCNT@CS-6 h. (g) Cycling stability of three different NCNT@CS samples. Copied with permission [36]. Copyright 2018, John Wiley & Sons. (h) SEM images of Se@NOPC-CNT. The inset is an optical image of free-standing Se@NOPC-CNT film. (i) TEM images of NOPC-CNT. (j) Long-term cycling performance and coulombic efficiency of the cathode. Copied with permission [37]. Copyright 2018, John Wiley & Sons.

stability. As a result, NCSCNT electrode demonstrated higher rate performance (75 mAh/g at 1000 mA/g) than that of graphite anodes in PIBs (failed at ~500 mA/g), and retained a capacity of 236 mAh/g after 100 cycles (Figs. 3c and d).

In order to further improve the capacity of CNT-based binder-free electrodes [33–35], Yu *et al.* designed a hybrid electrode with a metallic octahedral $CoSe_2$ threaded by N-doped multiwall CNTs (NCNT@CS) for PIBs, as shown in Figs. 3e-g [36]. The structural superiority lied in the synergistic promotion between transition metal chalcogenides (TMC) of high capacity and NCNT with flexible conductive network. The formation of core-shell wired structure greatly improved the electrical conductivity of TMC and alleviated the volume expansion upon K-ion intercalation. As expected, when used as the anode for PIBs, the unique hybrid structure delivered a high capacity (253 mAh/g at 0.2 A/g over 100 cycles) and enhanced rate performance (173 mAh/g at 2.0 A/g over 600 cycles).

In addition, multi-element doping in CNT-based materials can adjust their electronic and chemical properties, thereby improving the electrochemical performance. For example, the dual doping of N and O heteroatoms has been confirmed as an efficient way to modify the electronic structures of carbon materials *via* elevating their charge carrier density, surface energy and chemical affinity. As a demonstration, Yao's group reported for the first time a facile fabrication strategy to achieve a novel 3D flexible, multifunctional Se/C electrode configured by infiltration of Se in the CNT interwoven N, O dual-doped porous carbon nanosheets (Se@NOPC-CNT), which was utilized as the flexible free-standing cathode for K-Se batteries (Figs. 3h and i) [37].The electrode exhibited a long cycle life (335 mAh/g at 800 mA/g after 700 cycles), as shown in Fig. 3j. The highly porous but integrated NOPC-CNT framework has helped to load Se, buffer the stress induced by volume changes and ensure the high conductivity of the hybrid cathode.

2.3. Carbon nanofibers (CNFs) based free-standing electrodes

For the application in PIBs, free-standing CNF was usually synthesized by electrospinning method because of its versatility, controllability and high efficiency. 2D films of CNFs can be produced by the decomposition of various polymers (such as polyacrylonitrile (PAN), polyvinyl pyrrolidone (PVP), polyvinyl alcohol (PVA), pitch) directly on substrates with subsequent carbonization. When used as electrodes, the entire 2D surface with interconnected CNFs is accessible by electrolyte ions, enabling fast charge storage [38,39]. In general, such 2D structures can provide high in-plane electronic conductivity, but the conductivity in the out-of-plane direction is basically relatively inferior due to the limited contact of each CNFs. So far, a series of modified CNFs-based electrodes including nanoporous CNFs [40–42] and nitrogen-doped CNFs (N-CNFs) [43–45] have been proposed to further increase the ion diffusion and electron transport within the entire electrode film; hybrid electrodes such as ultra-small antimony nanocrystals incorporated composite CNFs (Sb@CNFs) [46] were also developed to boost the capacity of electrodes.

Zhao's group fabricated free-standing 3D porous CNFs paper anodes by electrospinning and subsequent pyrolysis (Fig. 4a) [42]. The porous structure can effectively alleviate the volume expansion induced by the insertion of large K^+, and enable easy infiltration of electrolyte and short diffusion pathway of K^+. Exactly due to these features, the electrode demonstrated good rate capability; the specific capacity reached 275 mAh/g at 20 mA/g and 100 mAh/g at 7700 mA/g (Fig. 4b). The elemental doping and defect strategies were also adopted for a wide range of CNFs [46]. Ryan A Adams's group reported the effect of oxygen functionalization on K-ion carbon anode performance for the first time *via* plasma oxidation of the prepared free-standing CNFs (Fig. 4c) [45].

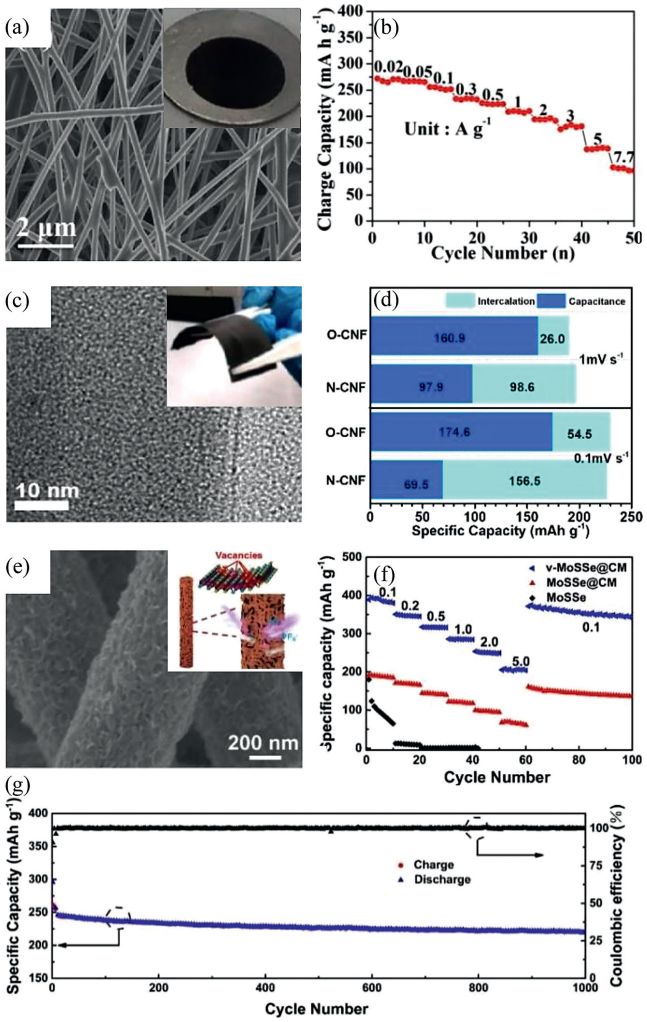

Fig. 4. (a) SEM image of CNF film. Inset is the digital photograph of the cycled CNF anode. (b) Rate performance of the porous CNF anode. Copied with permission [42]. Copyright 2017, The Royal Society of Chemistry. (c) TEM image of plasma-oxidized CNF and the inset is flexible binder-free N-CNF mat. (d) The contributions of surface and intercalation charge storage processes for different samples. Copied with permission [45]. Copyright 2017, American Chemical Society. (e) SEM image and detailed structural illustration of v-MoSSe@CM anode. (f) Rate performance comparison of the v-MoSSe@CM, MoSSe@CM and MoSSe anodes. (g) Cycling performance of v-MoSSe@CM at a high current density of 0.5 A/g. Copied with permission [49]. Copyright 2019, Elsevier B.V.

As shown in Fig. 4d, compared with N-CNFs, oxygen functionalization did not significantly increase the total capacity, but the surface charge storage percentage did increase, indicative of faster kinetics enabled by the incorporation of oxygen.

High-capacity electrode materials have also been hybridized with CNFs and directly used in PIBs without binders and additives [47–53]. For example, Tian's group reported a flexible free-standing hybrid anode that was designed by anchoring dual anionic vacancy-rich MoSSe arrays on an electrospun CNFs membrane(v-MoSSe@CM) [49] (Fig. 4e). The introduced dual anionic vacancies in v-MoSSe arrays can enhance the adsorption ability of K^+ and promote the electron transfer. Therefore, the v-MoSSe@CM anode exhibited a higher capacity of 370.6 mAh/g at 0.1 A/g over 60 cycles than that of MoSSe@CM (168.5 mAh/g), as illustrated in Fig. 4f. The unique 3D networks of CM could further buffer the volume expansion of v-MoSSe during the conversion reaction and stabilize the integral structure. Consequently, the v-MoSSe@CM anode still retained a specific capacity of 220.5 mAh/g after 1000cycles at 0.5 A/g, with a capacity fading of only 0.015% per cycle (Fig. 4g).

As demonstrated above, a variety of free-standing CNF-based electrode materials with light weight, high chemical stability and good mechanical property have been successfully developed for PIBs. However, CNFs typically have low graphitization degree as compared to graphene and CNTs, which makes pristine CNFs less conductive and gives rise to relatively small reversible capacity [16]. To further manifest the advantages of CNFs as free-standing substrates for PIBs, the post-treatment temperature and atmosphere can be controlled to improve the graphitization. In addition, the diameter of most reported CNFs was relatively large; future studies can also be focused on decreasing the CNF diameter to help increase the loading amount of other active materials in CNF film.

3. Substrate-assisted methods towards binder-free electrodes

3.1. Stainless steels mesh (SSM)-based substrates

SSM substrates possess a 3D knitted mesh structure and certain flexibility, thus they are usually adopted to grow various arrays/films to form binder-free electrodes. In these cases, SSMs act not only as skeleton to support the growth of active materials, but also as current collector due to the outstanding electronic conductivity [54]. The nanoarrays/films of active materials can be grown on SSMs *via* well-defined chemical and physical methods. Such a direct growth is beneficial from the surface chemistry and nanosized roughness of the surface of metal substrates [18,21].

For example, using rusty stainless steels mesh (RSSM) as solid-state iron sources and conductive substrates, Zhu *et al*. developed a facile way to fabricate flexible binder-free cathode *via in situ* transforming the corrosion layer of RSSM into compact stack layer of Prussian Blue nanocubes (PB@SSM), as displayed in Figs. 5a and b [55]. Moreover, to further enhance conductivity and improve structural stability of PB@SSM electrode, a unique rGO coated structure (rGO@PB@SSM) was designed (Figs. 5c and d). In this cathode structure, rGO films were tightly adhered to each nanocube, indicative of an intimate and robust contact with PB nanocubes. Such a unique structure not only avoided the agglomeration of active materials and the detachment of the materials from SSM during cycling, but also ensured ultrafast electron transport within the cathode. As displayed in Fig. 5e, when used as cathode in PIBs, the RGO@PB@SSM delivered a discharge capacity of 84, 60 and 43 mAh/g at a current density of 50, 200 and 400 mA/g, respectively, and exhibited a better cycle stability (71.8% capacity retention after 305 cycles at 100 mA/g) compared to PB@SSM (Figs. 5f and g).

Actually, commercial SSMs with different pore sizes and pore volumes are available on the market. The loading mass and active materials structure on SSMs can be readily tuned by choosing different kind of SSMs and controlling the experimental parameters, which is critical to optimize the device performance and thus deserves in-depth studies in future. In addition, besides SSMs, meshes of other metals such as nickel, titanium and copper are promising as substrates to directly grow nanoarrays or films for advanced PIBs.

3.2. MXene-based substrates

MXene offers quite unique combination of 2D architecture, excellent mechanical properties, hydrophilicity, metallic conductivity and superb intercalation with other materials [56]. Like graphene and CNTs, it could be easily assembled into additive-free and free-standing substrates, demonstrating high mechanical stability and flexibility. Moreover, various mono- or multivalent cations (*e.g*., Li^+, K^+, Zn^{2+} and Al^{3+}) can easily intercalate into MXenes sheets and occupy electrochemical active sites for energy storage. In this case, MXenes possess higher volumetric energy storage performance as compared to graphene and CNTs, due to its high materials density. In addition, diverse metals and metal compounds such as Bi, Sn and the related oxides can further grow on MXene substrate, forming binder-free hybrid electrodes for PIBs.

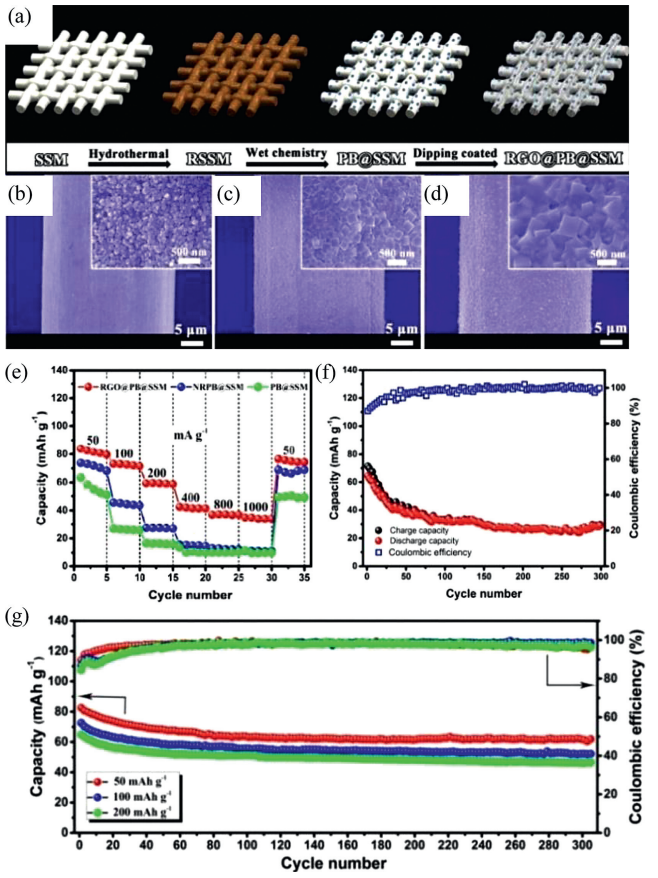

Fig. 5. (a) Schematic illustration for the synthesis of binder-free rGO@PB@SSM cathode. SEM images of (b) RSSM, (c) PB@SSM and (d) rGO@PB@SSM. (e) Rate capability of PB@SSM, PB@SSM reduced by potassium borohydride (NRPB@SSM) and rGO@PB@SSM. (f) Cycle performance of PB@SSM cathode at 100 mA/g. (g) Cycling performance of rGO@PB@SSM cathode at different current densities. Copied with permission [55]. Copyright 2017, John Wiley & Sons.

The high metallic electronic conductivity and low ion diffusion barrier generally endow MXene-based electrodes with high-rate ions storage. As shown in Fig. 6a, Tian's group constructed hierarchical porous Sb directly on MXene paper (MXene@Sb) *via* a universal one-step electrodeposition approach [57]. The cross-sectional SEM images and digital photograph are illustrated in Figs. 6b and c. As can be seen, MXene@Sb anode has perfectly integrated the unique properties of MXene and hierarchical porous Sb in a complementary way. Hierarchical porous Sb robustly grew on layered MXene paper, offering fast and accessible ion transport and providing a short diffusion distance for potassium ions. Consequently, this binder-free structure exhibited a reversible capacity of 516 mAh/g at 50 mA/g and a rate performance of 270 mAh/g at 500 mA/g (Fig. 6d). In order to better use MXene's sandwich structure, Zeng *et al*. integrated 2D materials into the sandwiched structures *via* vacuum filtration with the assistance of electrostatic attraction (Figs. 6e and f) [58]. By utilizing the negatively charged property of MXene and positively charged feature of GO-PDDA, they firstly assembled MXene with GO nanosheets and then transformed MXene into ultrathin titanate with well-confined layered structure in a confined fashion. During the transformation process, GO was also reduced into rGO. This

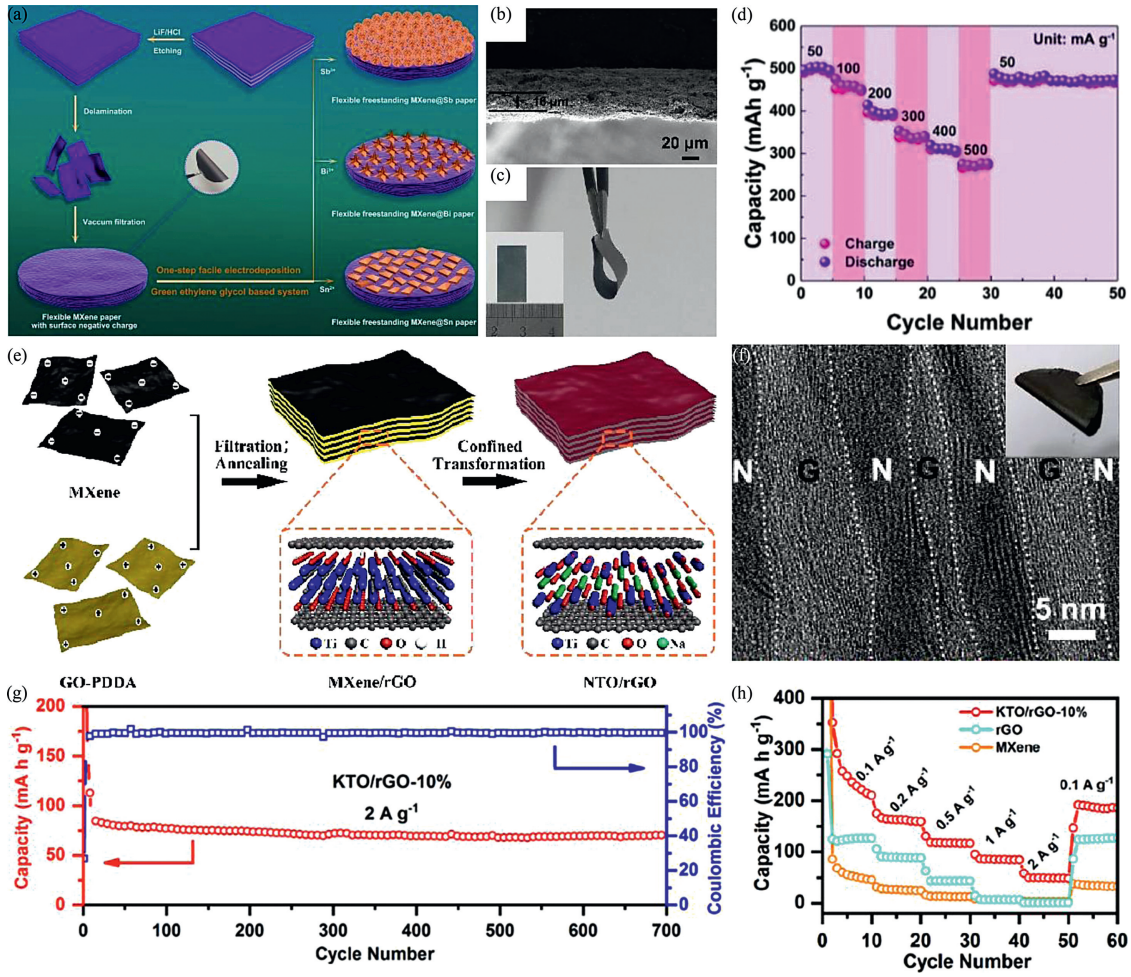

Fig. 6. (a) Schematic illustration of the fabrication process of binder-free MXene@Sb, MXene@Bi and MXene@Sn paper. (b)Cross-sectional SEM image of MXene@Sb. (c) Digital photograph of MXene@Sn paper. (d) Rate performance of MXene@Sb. Copied with permission [57]. Copyright 2019, the Royal Society of Chemistry. (e) The fabrication process of NTO/rGO films. (f) Cross-sectional TEM image of NTO/rGO ("N" refers to NTO, and "G" refers to rGO). (g) Long-term cycling performance of KTO/rGO-10%. (h) Rate performance comprasion of KTO/rGO-10%, rGO and MXene. Copied with permission [58]. Copyright 2018, John Wiley & Sons.

unique hybrid binder-free anode not only prevented restacking of few-layered nanosheets but also kept the ultrathin feature of the precursor of MXene. By contrast, the direct transformation of 2D MXene without any protection would easily destroy the ultrathin structure of 2D layered sodium titanate (NTO). The synthesis strategy is versatile and was further used to attain flexible potassium titanate (KTO)/rGO films, which demonstrated good cycling stability (with a capacity of 75 mAh/g after 700 cycles at 2 A/g, Fig. 6g) and reversible capacities of 228, 162, 116 and 84 mAh/g at the current densities of 0.1, 0.2, 0.5, 1 A/g, respectively (Fig. 6f).

Despite some progress, the controllable design and synthesis of MXene-based binder-free electrodes for PIBs as well as the fundamental understanding of relevant scientific issues remain challenging and need to be addressed. Due to the difficulties in understanding the regulation rule between surface metal species and the surface functional groups, existing surface modification techniques are still limited. With the theoretically clarification of the interaction between hybrid phase with MXene, we are confident that more and more attractive MXene-based hybrid binder-free electrode architectures will be developed experimentally in future for PIB application [59–61].

3.3. Metal/carbon foam-based substrates

Similar to aforementioned metal meshes, metal (Ni, Cu, *etc.*) and carbon-based foams have a highly porous structure with an interconnected 3D scaffold and are also regarded as an excellent template to *in situ* grow a variety of active electrode materials for PIBs [62–65]. Different from meshes, foams can be pre-pressed in most cases to reduce the volume while still having sufficient voids for active materials growth, which is beneficial for achieving higher volumetric capacity of electrodes and higher volumetric energy density of devices.

As a typical demonstration, Fei *et al.* constructed an all-solid-state potassium metal battery with a poly (ethylene oxide)-bis (flourosulfonyl)imide potassium based solid polymer electrolyte (SPE) and binder-free electrodes [66]. A 3D array-structured Ni_3S_2 was grown *in-situ* on Ni-foam by hydrothermal reaction and used as a binder-free high-capacity anode of PIBs. In this design, the array structure offered abundant active electrochemical-reaction site and the interconnected Ni foam acted as the conductive pathway for electron transport within the electrode, ensuring sufficient electrochemical reaction kinetics. As a result, the cell with PEO-based SPE exhibited a stable cycling performance with a discharge capacity of 307 mAh/g after 100 cycles.

Similarly, Suo's group for the first time developed a 3D N-doped carbon foam covered with ultrathin $CoSe_2$ nanosheets (CSNS/NCF) core/sheath framework as binder-free anode for high-performance potassium storage [67]. The intimate adhesion of $CoSe_2$ nanosheets sheath and N-doped carbon foam core was established through C-*N*-Co and C-Co bonds that were formed during solvothermal process. When evaluated as anode for PIBs, the optimized CSNS/

Table 2
Summary of binder-free electrodes for PIBs in terms of their electrode components, synthetic methods and electrochemical performance.

Substrate	Binder-free materials	Synthetic methods	Operating voltage range (V)	Electrochemical performance	Ref.
Free	rGO film	Hummer's method, chemical reduction	0.01–2	150 mAh/g at 10 mA/g after 175 cycles	[24]
	rGO/CNT	Vacuum filtration, thermal reduction	0.01–2.5	148 mAh/g at 50 mA/g after 200 cycles	[26]
	GO/FeP	Vacuum freeze-drying, anneal	0.01–3	97.6% retention at 2000 mA/g after 2000 cycles	[27]
	Sn@rGO	Vacuum freeze-drying, thermal reduction	0.01–3	123 mAh/g at 500 mA/g after 1500 cycles	[28]
	NCSCNT	CVD	0.01–2.5	236 mAh/g at 20 mA/g after 100 cycles	[32]
	sulfur-mediated GO aerogel	Hydrothermal, anneal	0.01–3	320 mAh/g at 100 mA/g after 500 cycles	[33]
	$Na_xV_2O_5{\cdot}nH_2O$/rGO/CNT	Hydrothermal, vacuum filtration	1.5-3.8	59.7 mAh/g at 500 mA/g after 600 cycles	[34]
	CNT@PB	Liquid-liquid interfacial method, electrochemical deposition	0.01-0.8	74% retention at 10.82 $\mu A/cm^3$ after 1000 cycles	[35]
	N-doped $CoSe_2$@CNTs	CVD, hydrothermal	0.01–2.6	173 mAh/g at 2000 mA/g after 600 cycles	[36]
	N,O dual-doped Se@CNTs	Melt diffusion method	0.5-3	400 mAh/g at 1000 mA/g after 2000 cycles	[37]
	Coal liquefaction residues-based NFs	Electrospinning, carbonization	0.01–3	98% retention at 50 mA/g after 320 cycles	[40]
	Multichannel carbon fibers	Electrospinning	0.01–3	110.9 mAh/g at 2000 mA/g after 2000 cycles	[41]
	Porous CNFs	Electrospinning, carbonization	0-3	270 mAh/g at 200 mA/g after 1200 cycles	[42]
	PNCFs	Electrospinning, carbonization	0.01–3	65 mAh/g at 100 mA/g after 346 cycles	[43]
	pyrrolic/pyridinic-N-doped hollow carbon	Electrospinning, pyrolysis	0-2.6	161.3 mAh/g at 1000 mA/g after 1600 cycles	[44]
	N-doped CNFs	Electrospinning, carbonization, plasma cleaner	0.005–3	170 mAh/g at 1 C after 1900 cycles	[45]
	N-doped P@CNFs	Electrospinning	0.01–2	465 mAh/g at 2000 mA/g after 800 cycles	[8]
	Ultrasmall-Sb@CNFs	Electrospinning, carbonization	0.01–3	225 mAh/g at 1000 mA/g after 2000 cycles	[46]
	$NiCo_2S_4$@N-hollow CNFs	Electrospinning, carbonization	0.01–3	134.3 mAh/g at 3200 mA/g after 600 cycles	[47]
	MoP@NP-CNFs	Electrospinning, carbonization	0.01–3	220 mAh/g at 2000 mA/g after 200 cycles	[48]
	MoSSe@CNFs membrane	Electrospinning, anneal	0.01–3	220.5 mAh/g at 0.5 mA/g after 1000 cycles	[49]
	$Co_{0.85}Se$@carbon nanoboxes@CNFs	Electrospinning, carbonization	0.01–2.6	299 mAh/g at 1000 mA/g after 400 cycles	[51]
	Free-standing CNTs@CNFs	Electrospinning	0.01–2	193 mAh/g at 1 C after 300 cycles	[52]
	N-doped ReS_2@CNFs	Electrospinning, hydrothermal	0.01–3	253 mAh/g at 50 mA/g after 100 cycles	[53]
SSM	SnO_2@SSM	Hydrothermal	0.01–2.6	128 mAh/g at 1000 mA/g after 200 cycles	[54]
	rGO@PB@SSM	In situ transforming, rGO coated	2-4	75.1% retention at 1000 mA/g after 305 cycles	[55]
MXene	MXene@Sb	Electrodeposition	0.01–1.2	398 mAh/g at 500 mA/g after 500 cycles	[56]
	KTO/rGO	Hydrothermal	0-2.5	75 mAh/g at 2000 mA/g after 700 cycles	[57]
CF	SnO_2@CF	Electrodeposition	0.01–3	231.7 mAh/g at 1000 mA/g after 400 cycles	[62]
	CNTs/CF	CVD, hydrothermal	0.05-2	127 mAh/g at 500 mA/g after 2000 cycles	[63]
	CSNS/NCF	Hydrothermal	0.01–2.5	335 mAh/g at 50 mA/g after 200 cycles	[67]
Cu-Foam	C/Cu	Hydrothermal, anneal	0.01–3	129 mAh/g at 2000 mA/g after 20000 cycles	[64]
CS	$Na_2Ti_3O_7$@N-doped CS	Pyrolysis, hydrothermal	0-2.6	114 mAh/g at 100 mA/g after 1555 cycles	[65]
Ni-Foam	Ni_3S_2	Hydrothermal	0.01–3	307 mAh/g at 25 mA/g after 100 cycles	[66]
CC	N, P-vertical grapheme@CC	Microwave plasma-enhanced chemical vapor deposition, anneal	0.01–3	82% retention at 25 mA/g after 1000 cycles	[68]
Paper	CTPB@paper	Cyanotype process	2-4.5	58.5 mAh/g at 200 mA/g after 500 cycles	[69]

CF: carbon foam, SnO_2@CF: SnO_2@carbon foam, CS: carbon sponge, PNCF: porous N-doped carbon fibers.

NCF showed a high capacity of 335 mAh/g after 200 cycles at 50 mA/g; a capacity of 198 mAh/g can still be kept even at 1000 mA/g after 1000 cycles.

3.4. Other substrates for binder-free electrodes

Although the substrates discussed above were mainly used to fabricate binder-free electrodes for PIBs, some demerits of these substrates cannot be ignored, such as the high cost of MXenes and carbon foams, and the relatively heavy weight of metal-based substrates. In addition, it is still challenging in ensuring close contact between active materials and the substrates during repeated shape deformations (such as bending, twisting and stretching), under which conditions stress will be continuously generated and released. So for the direct growth/deposition of binder-free electrodes of PIBs, other substrates have also drawn attention, those include carbon-based (*e.g.*, carbon cloth (CC), carbon paper) ones, Xuan paper and textiles [68].

For instance, with the use of Xuan paper as substrate, Zhu *et al.* proposed cyanotype as a novel photographic printing strategy for the fabrication of low-cost, lightweight and flexible binder-free electrodes by the photoinduced synthesis of highly crystalline PB nanocubes (CTPB) [69]. Firstly, they immersed a piece of Xuan paper in the photosensitizer solution (potassium ferricyanide solution mixed with ferric ammonium citrate) to form daylight paper. Subsequently, the photosensitizer solution is directly irradiated with UV light, causing the Fe^{3+} ions in ferric ammonium citrate to be reduced to Fe^{2+} ions. Finally, the few generated Fe^{2+} ions are immediately consumed by excess ferricyanide ions to form CTPB accompanied by the simultaneous color change to dark green. Coin cells with metallic K counter electrodes were assembled, and the galvanostatic discharge/charge technique was employed to evaluate the electrochemical performance. As the current densities increase from 50 mA/g to 100, 200, 400 and 500 mA/g, the CTPB electrode delivers good capacity retention, varying from 109 mAh/g to 107, 97, 88 and 84 mAh/g, respectively. This appealing photographic printing technique as well as the excellent electrochemical results opened a new avenue for the large-scale fabrication of flexible energy storage devices. Inspired by this, other insulating substrates such as textiles can also be

treated by coating conductive carbon slurry or silver slurry for subsequent deposition of active materials to form binder-free PIB electrodes [70,71].

4. Conclusions and perspectives

In this review, we have briefly presented recent progress in the design and fabrication of binder-free electrodes for PIBs. The typical electrodes, preparation methods and electrochemical performance are summarized in Table 2. To sum up, designing free-standing electrodes and growing active materials directly on current collector substrates are two major ways to fabricating binder-free electrodes. For free-standing electrodes design, carbon-based materials including 1D fibers or yarns, 2D sheets and 3D foams and their composites can be used either as conductive materials or active materials; they can be combined with other active materials (such as PB, Sn, Se) to enable the development of various free-standing configurations (such as paper-like, textile, sponge), which generally have higher capacity, better rate capability and superior cycle stability than the individual counterparts. To directly grow the binder-free electrodes, metal substrates (Cu, Ti, Ni, SSM, carbon sponge, paper, *etc.*), carbon-based substrates, and even treated papers and textiles with appropriate conductivity are promising to support the growth or deposition of active materials. In most cases, the as-prepared binder-free electrodes also possess good flexibility, which is critical to future application in flexible electronics.

Despite the considerable progress, this research area is still in its infancy and there are some challenges need to be addressed before realizing the practical applications. Looking into the future, the following directions can be considered for the design of binder-free electrodes and PIBs:

(1) New binder-free electrode substrates. Novel substrates, which not only have great flexibility but also demonstrate excellent stretchability and compressibility, are quite attractive to develop advanced multifunctional binder-free electrodes. In combination with stretchable electrolytes and packing materials, the resulting stretchable PIBs will show great promise as power sources for future wearable electronics.

(2) Flexible full-cell design. Till now, most of the binder-free electrodes for PIBs are anodes in literatures; binder-free cathodes are quite rare as they are typically ternary or even multielemental and thus not easy to directly grow. To realize effective full-cell assembly, it is highly necessary to develop more kinds of free-standing or directly grown cathodes and further choose appropriate cathode-anode couples as well as realize good charge balance between the two binder-free electrodes.

(3) Explore novel electrolytes with good flexibility. Conventional flammable liquid electrolytes are high-cost, unsafe and easy to leak. They also flow inside during battery shape deformation, significantly affecting the device performance. By contrast, (*quasi*-) solid-state electrolytes, especially gel or polymer electrolytes, can provide better safety, integrity and compatibility. Thus, searching for such solid-state electrolytes with comparable ionic conductivity to liquid electrolyte becomes an urgent issue to be solved.

(4) Systematically evaluate the flexibility of binder-free electrodes. In addition to presenting the simple electrochemical cyclic voltammetry (CV) and galvanostatic charge–discharge (GCD) curves under deformable states, more detailed data in terms of other electrochemical attributes (such as battery voltage, polarization, impedance spectrum, capacity and self-discharge) under the continuous and dynamic deformation of the electrode should be reported and analyzed. It is also necessary to quantitatively report bending curvatures and the related tensile strains. These metrics are of great importance to assess the application potential of binder-free electrodes for flexible PIBs.

(5) Low-cost and scalable production of binder-free electrodes. Exploring large-scale and industrial production technologies to lower the fabrication cost is urgent. Mature techniques such as the aforementioned printing and cyanotype processes are promising for the economical fabrication of binder-free electrodes. Other new potential techniques can be further developed in the lab research with the consideration of choosing low-cost precursor materials and inexpensive chemical/physical reaction systems.

(6) Integration of binder-free PIBs with other devices. For example, the combination of PIBs with energy harvesting devices such as solar cells is capable of achieving self-powering devices. These integrated devices combining different functions show great potential in future portable and wearable electronics.

The successful realization of binder-free full-cell PIBs critically relies on the innovations in binder-free electrode materials, flexible electrolytes and effective full-cell assembly techniques. Encouraged by the considerable progress in this field, it is envisioned that in the future, binder-free electrodes and PIBs will play important roles in inexpensive and sustainable electrochemical energy storage.

Declaration of competing interest

The authors declare that they have no known competing financial interests or personal relationships that could have appeared to influence the work reported in this paper.

Acknowledgments

This work was supported by the National Natural Science Foundation of China (Nos. 51972257, 51672205 and 51872104) and the National Key R&D Program of China (No. 2016YFA0202602).

References

[1] Q. Zhang, Z. Wang, S. Zhang, et al., Electro. Ener. Rev. 1 (2018) 625–658.
[2] J. Zhang, T. Liu, X. Cheng, et al., Nano Energy 60 (2019) 340–361.
[3] M. Li, L. Xiao, D. Wang, et al., Chin. Chem. Lett. 12 (2019) 2328–2332.
[4] C. Zhang, H. Zhao, Y. Lei, Energy Environ. Mater. 3 (2020) 105–120.
[5] W. Wei, B. Ding, H. Dou, et al., Chin. Chem. Lett. 30 (2019) 2110–2122.
[6] J.C. Pramudita, D. Sehrawat, D. Goonetilleke, N. Sharma, Adv. Energy Mater. 7 (2017) 1602911.
[7] W.C. Zhang, Y.J. Liu, Z.P. Guo, Sci. Adv. 5 (2019) 7412.
[8] A. Eftekhari, Z. Jian, X. Ji, ACS Appl. Mater. Interfaces 9 (2017) 4404–4419.
[9] X. Li, H. Wang, W. Zhang, et al., Acta Metall. Sin. (Engl. Lett.) 33 (2020) 1–8.
[10] Y.S. Xu, S.Y. Duan, Y.G. Sun, et al., J. Mater. Chem. A 7 (2019) 4334–4352.
[11] C. Vaalma, D. Buchholz, S. Passerini, Curr. Opin. Electrochem. 9 (2018) 41–48.
[12] S. Komaba, T. Hasegawa, M. Dahbi, K. Kubota, Electrochem. Commun. 60 (2015) 172–175.
[13] Z. Jian, Z. Xing, C. Bommier, Z. Li, X. Ji, Adv. Energy Mater. 6 (2016) 1501874.
[14] Y. Wu, S. Hu, R. Xu, et al., Nano Lett. 19 (2019) 1351–1358.
[15] H. Kim, J.C. Kim, M. Bianchini, et al., Adv. Energy Mater. 8 (2018) 1702384.
[16] T. Jin, Q. Han, L. Jiao, Adv. Mater. 32 (2020) 1806304.
[17] S.H. Qi, J.W. Deng, W.C. Zhang, et al., Rare Met. 39 (2020) 970–988.
[18] J. Jiang, Y. Li, J. Liu, et al., Adv Mater. 24 (2012) 5166–5180.
[19] R. Fang, S. Zhao, Z. Sun, et al., Adv Mater. 29 (2017) 1606823.
[20] J. Ji, Y. Li, W. Peng, et al., Adv Mater. 27 (2015) 5264–5279.
[21] J. Jiang, Y. Li, J. Liu, X. Huang, Nanoscale 3 (2011) 45–58.
[22] H. Ahmad, M. Fan, D. Hui, Compos. B: Eng. 145 (2018) 270–280.
[23] Q. Ke, J. Wang, J. Materiomics 2 (2016) 37–54.
[24] W. Luo, J. Wan, B. Ozdemir, et al., Nano Lett. 15 (2015) 7671–7677.
[25] X. Wu, Y. Chen, Z. Xing, et al., Adv. Energy Mater. 9 (2019) 1900343.
[26] S. Peng, L. Wang, Z. Zhu, K. Han, J. Phys. Chem. Solid. 138 (2020) 109296.
[27] Z. Zhang, C. Wu, Z. Chen, et al., J. Mater. Chem. A 8 (2020) 3369–3378.
[28] H. Wang, Z. Xing, Z. Hu, et al., Appl. Mater. Today 15 (2019) 58–66.
[29] P. Zhang, Z. Li, S. Zhang, G. Shao, Energy Environ. Mater. 1 (2018) 5–12.
[30] F. Li, Z. Yu, X. Han, R.Y. Lai, Anal. Chim. Acta 1051 (2019) 1–23.
[31] T. Tao, S. Lu, Y. Chen, J. Adv. Mater. Technol. 3 (2018) 1700375.
[32] X. Zhao, Y. Tang, C. Ni, et al., ACS Appl. Energy Mater. 1 (2018) 1703–1707.
[33] Y. Zhao, J. Ruan, S. Luo, et al., ACS Appl. Mater. Interfaces 11 (2019) 40006–40013.
[34] G. Xu, X. Liu, S. Huang, et al., ACS Appl. Mater. Interfaces 12 (2020) 706–716.
[35] E. Nossol, V.H.R. Souza, A.J.G. Zarbin, J. Colloid Interface Sci. 478 (2016) 107–116.
[36] Q. Yu, B. Jiang, J. Hu, et al., Adv. Sci. 5 (2018) 1800782.

[37] Y. Yao, M. Chen, R. Xu, et al., Adv. Mater. 30 (2018) 1805234.
[38] M. Inagaki, Y. Yang, F. Kang, Adv. Mater. 24 (2012) 2547–2566.
[39] P. Zhou, X. Wang, W. Guan, et al., ACS Appl. Mater. Interfaces 9 (2017) 6979–6987.
[40] X. Li, N. Sun, X. Tian, et al., Energy Fuels 34 (2020) 2445–2451.
[41] Y. Xu, T. Yuan, Y. Zhao, et al., Adv. Mater. Interfaces 7 (2019) 1901829.
[42] X. Zhao, P. Xiong, J. Meng, et al., J. Mater. Chem. 5 (2017) 19237–19244.
[43] M. Zhang, M. Shoaib, H. Fei, et al., Adv. Energy Mater. 9 (2019) 1901663.
[44] W. Yang, J. Zhou, S. Wang, et al., Synth. Environ. Sci. 12 (2019) 1605–1612.
[45] R.A. Adams, J.M. Syu, Y. Zhao, C.T. Lo, A. Varma, ACS Appl. Mater. Interfaces 9 (2017) 17872–17881.
[46] X. Xie, S. Qi, D. Wu, et al., Chin. Chem. Lett. 31 (2020) 223–226.
[47] X. Ge, S. Liu, M. Qiao, et al., Angew. Chem. Int. Ed. 58 (2019) 14578–14583.
[48] W. Zhang, J. Chen, Y. Liu, et al., J. Alloys. Compd. 823 (2020) 153613.
[49] Z. Yi, Y. Liu, Y. Li, et al., Small 16 (2020) 1905301.
[50] Z. Tian, N. Chui, R. Lian, et al., Energy Storage Mater. 27 (2020) 591–598.
[51] C. Atangana Etogo, H. Huang, H. Hong, G. Liu, L. Zhang, Energy Storage Mater. 24 (2020) 167–176.
[52] C. Shen, K. Yuan, T. Tian, et al., ACS Appl. Mater. Interfaces 11 (2019) 5015–5021.
[53] M. Mao, C. Cui, M. Wu, et al., Nano Energy 45 (2018) 346–352.
[54] G. Suo, D. Li, L. Feng, et al., J. Electroanal. Chem. 833 (2019) 113–118.
[55] Y.H. Zhu, Y.B. Yin, X. Yang, et al., Angew. Chem. Int. Ed. 56 (2017) 7881–7885.
[56] Q. Yang, Y. Wang, X. Li, et al., Energy Environ. Mater. 1 (2018) 183–195.
[57] Y. Tian, Y. An, S. Xiong, J. Feng, Y. Qian, J. Mater. Chem. A 7 (2019) 9716–9725.
[58] C. Zeng, F. Xie, X. Yang, et al., Angew. Chem. Int. Ed. 57 (2018) 8540–8544.
[59] H. Yu, Y. Wang, Y. Jing, et al., Small 15 (2019) 1901503.
[60] D. Er, J. Li, M. Naguib, Y. Gogotsi, V.B. Shenoy, ACS Appl. Mater. Interfaces 6 (2014) 11173–11179.
[61] J. Halim, S. Kota, M.R. Lukatskaya, et al., Adv. Func. Mater. 26 (2016) 3118–3127.
[62] H. Qiu, L. Zhao, M. Asif, et al., Energy Environ. Sci. 13 (2020) 571–578.
[63] S. Zeng, X. Zhou, B. Wang, et al., J. Mater. Chem. A 7 (2019) 15774–15781.
[64] Y. An, Y. Tian, Y. Li, S. Xiong, G. Zhao, et al., J. Mater. Chem. A 7 (2019) 21966–21975.
[65] P. Li, W. Wang, S. Gong, et al., ACS Appl. Mater. Interfaces 10 (2018) 37974–37980.
[66] H. Fei, Y. Liu, Y. An, et al., J. Power Sources 433 (2019) 226697.
[67] G. Suo, J. Zhang, D. Li, et al., Chem. Eng. J. 388 (2020) 124396.
[68] W. Qiu, H. Xiao, Y. Li, X. Lu, Y. Tong, Small 15 (2019) 1901285.
[69] Y.H. Zhu, X. Yang, D. Bao, et al., Joule 2 (2018) 736–746.
[70] L. Nayak, S. Mohanty, S.K. Nayak, A. Ramadoss, J. Mater. Chem. C 7 (2019) 8771–8795.
[71] Q. Huang, Y. Zhu, J. Adv. Mater. Technol. 4 (2019) 1970029.